# Resolving the effects of 2D versus 3D grain measurements on (U-Th)/He age data and reproducibility

Emily H. G. Cooperdock[1,2], Richard A. Ketcham[1], Daniel F. Stockli[1]

[1]Department of Geological Sciences, University of Texas at Austin, Austin, 78712, USA
5  [2]Woods Hole Oceanographic Institution, Woods Hole, 02543, USA

*Correspondence to*: Emily H. G. Cooperdock (ecooperdock@whoi.edu)

**Abstract.** (U-Th)/He thermochronometry relies on accurate and precise quantification of individual grain volume and surface area, which are used to calculate mass, alpha ejection ($F_T$) correction, isotope concentrations, equivalent sphere radius (ESR), and ultimately age. The vast majority of studies use 2D or 3D microscope dimension measurements and an
10  idealized grain shape to calculate these parameters, and a long-standing question is how much uncertainty these assumptions contribute to observed intra-sample age dispersion and accuracy. Here we compare the results for volume, surface area, grain mass, ESR, effective uranium (eU) and $F_T$ correction derived from 2D microscope and 3D x-ray computed tomography (CT) length and width data for >100 apatite grains. We analyzed apatite grains from two samples that exhibited a variety of crystal habits, some with inclusions. We also present 83 new apatite (U-Th)/He ages to assess the influence of 2D versus 3D $F_T$
15  correction on sample age precision. The data illustrate that the 2D approach systematically overestimates grain volumes and surface areas by 20-25%, impacting the estimates for mass, eU, and ESR – all important parameters used for interpreting age scatter and inverse modeling. $F_T$ factors calculated from 2D and 3D measurements differ by ~2%. This variation, however, has effectively no impact on reducing intra-sample age reproducibility. We also present a grain mounting procedure for x-ray CT scanning that can allow 100's of grains to be scanned in a single session, and new software capabilities for 3D $F_T$ and $F_T$-
20  based ESR calculations that are robust for relatively low-resolution CT data, that together enable efficient and cost-effective CT-based characterization.

## 1 Introduction

(U-Th)/He thermochronometry of accessory phases, such as apatite and zircon, has been widely applied to study
25  tectonic, volcanic, and surface processes. The method is based on the radiogenic accumulation of He from the alpha decay of U, Th, and Sm isotopes and the diffusive loss of He via thermal processes. In addition, He is lost due to 'long alpha stopping distances' associated with the kinetic energy of alpha decay (~5 MeV), requiring a shape-based alpha ejection correction ($F_T$ correction) (Farley et al., 1996). This correction as traditionally applied includes several simplifications and assumptions, such as an idealized grain geometry and homogenous parent nuclide concentrations (Farley et al., 1996, 2002; Ketcham et al.

2011). It has been shown that due to uncertainties in grain geometry, stopping distances, and parent nuclide zonation/variability, this correction can contribute >50% of the total analytical uncertainty (Farley and Stockli, 2002). The observation that the scatter of measured ages in even well-understood samples exceeds expectation based on analytical errors, combined with the knowledge that the above simplifications will not always hold, has led to the practice of reporting

5   errors derived from the reproducibility of standards rather than propagated analytical uncertainties in He dating. While the effect and mitigation of parent nuclide zonation in apatite and zircon to improve the accuracy and precision of (U-Th)/He ages has been studied, (e.g., Farley et al., 1996; Hourigan et al. 2005; Ketcham et al. 2011, Gautheron et al., 2011; Bargnesi et al., 2016), the effects of grain morphology and measurement on age, uncertainty, and intra-sample variability are less known.

10      In practice, for the determination of a correct He age, the grain dimensions and shape must be measured to compute a $F_T$ correction factor prior to He and U, Th, and Sm analysis, assuming either parent nuclide homogeneity or prescribing an assumed or measured 1D or 2D parent nuclide zonation. While not directly related to the computation of He ages, these same grain dimensions are also used to calculate grain size parameters, such as volume, surface area, and equivalent spherical radius (ESR) for the purpose of calculating isotopic/elemental concentrations and for age interpretation and diffusion or

15   thermal history modeling. For example, the grain mass, which is used to calculate the grain U, Th, Sm and He concentrations, is derived from the grain volume and an assumed density. Similarly, correlation between grain size (ESR) and He aliquot age is used for qualitative and quantitative thermal history reconstruction. Thus, the ability to measure accurate and precise grain dimensions, volumes, and surface areas for mineral grains has cascading effects for the determination, reporting, and interpretation of (U-Th)/He data.

20      Most commonly, $F_T$, volume, and surface area are calculated using 2 or 3 grain dimensions (length + width ± height) measured in 2D on an optical microscope using imaging software with a micrometer-based calibration. This approach requires the assumption of an idealized grain shape that most closely matches the mineral habit, such as a hexagonal prism for apatite or tetragonal prism for zircon, while simplifying (or ignoring) the more complex grain terminations. Hence, it has been best practice to select euhedral mineral grains to most closely match assumed, idealized

25   grain shapes and large grains to minimize the amplification of uncertainties related to the $F_T$ correction. However, even in felsic magmatic samples with high-quality apatite, grains are often characterized by a wide range of grain shapes, variations in grain terminations, and the potential for broken or chipped surfaces that cause deviations from the idealized hexagonal prism. Furthermore, apatite grains often do not represent symmetric or equidimensional hexagonal prisms and are characterized by varying face widths, commonly, but also possibly inconsistently, lying on their flattest face on the

30   microscope slide and thus potentially introducing systematic biases during the selection of the clearest, inclusion-free grains.

Recognizing that this optical-microscopy approach is both limiting and may be an important source for error or bias in (U-Th)/He ages and their interpretation, more sophisticated approaches have been proposed to determine grain dimensions, namely methods that do not require assuming a grain shape (Herman et al., 2007; Evans et al., 2008; Glotzbach et al., 2019). One approach presented by Glotzbach and others (2019), called "3DHe", is an openly available software that

uses orthogonal 2D grain photos to model accurate 3D grain shapes. Others have employed x-ray computed tomography (CT) to determine accurate grain shapes in an effort to improve precision and accuracy in $F_T$ and (U-Th)/He age determinations. Herman and others (2007) used 3D CT grain dimensions to calculate $F_T$ factors and present a production-diffusion model to extract thermal histories for detrital apatite grains. Evans and others (2008) tested the efficacy of 2D
5    microscope measurements against 3D CT data of zircon and apatite grain shape and size and documented a 1-24% discrepancy in derived $F_T$ values between microscope measurements and the CT data for even simple shapes (e.g., sphere).

This new study investigates the effect of 2D versus 3D grain geometry measurement techniques on grain dimension, volume, surface area, ESR, mass, $F_T$ and the corrected age as well as effective uranium (eU) concentrations. In contrast to previous studies, we characterized >100 apatite grains from two granitic samples for a more statistically robust comparison
10    and in an effort to more systematically capture variations in apatite morphologies, sizes, and screen for inclusions. The apatite grains were picked and measured by a single analyst using 2D optical techniques and then CT-scanned. Building on previous work, we present a method for relatively rapid scans of >100 grains at 4-5 µm resolution, enabling affordable and efficient 3D screening. We introduce the capabilities of an updated version of Blob3D (Ketcham 2005; freely distributed software) that allows efficient batch processing of CT-scanned grains and outputs parameters such as grain volume and 3D
15    $F_T$. We further develop an approach for calculating ESR on the basis of equivalent-$F_T$ rather than an equivalent surface-to-volume ratio as a more direct and accurate means of approximating the diffusional domain as a sphere. Finally, in contrast to previous studies, we use the results of >80 apatite (U-Th)/He ages to evaluate the reliability of the 2D measurements as well as the impact on the (U-Th)/He age and uncertainty.

### 1.1 Geologic background of the samples

20    For this study, we selected two plutonic samples from the Cretaceous Cordilleran magmatic arc in the western USA that yielded abundant, high-quality apatite and have been part of previous thermochronometric studies. Sample 97BS-CR8 is from a granodiorite in the Carson Range in the eastern Sierra Nevada along the Nevada-California border. The sample yielded an apatite fission track age of 68 ± 2 Ma (Surpless et al., 2002). The second sample, 95BS-11.3 is from a quartz monzonite exposed in the Wassuk Range in western Nevada, exhumed during Basin and Range normal faulting. The sample
25    has a reported apatite fission track age of 16.3 ± 1.4 Ma and apatite (U-Th)/He age of 9.9 ± 1.9 Ma (Stockli et al., 2002). These samples were chosen for their abundant apatite and relatively simple cooling histories. Their geologic histories are relevant to the present study in that the apatite grains derive from plutonic rocks and did not experience complex metamorphic or magmatic histories, nor natural abrasion during sedimentary transport. Furthermore, both samples derive from plutons that experienced rapid post-magmatic cooling or fault-related exhumation and are expected to have spent little
30    time in the apatite He partial retention zone and therefore should be less affected by slow cooling which would amplify kinetic effects on age dispersion.

## 2 Methods

### 2.1 Grain selection and 2D measurements

62 and 50 apatite grains were picked dry using a Nikon SMZ-U/100 optical microscope at a total magnification of 180x from two samples (97BS-CR8 and BS95-11.3). Apatite grains were selected to include the range of grain morphologies present in the sample (e.g., broken, flat, and prismatic ends). Intentionally, several grains with visible inclusions were also selected. All apatite grains were photographed using a Nikon digital ColorView camera connected to the microscope. The short and long axes were measured manually using AnalySIS® imaging software (Figure 1 and 3). For sample BS95-11.3, grains were imaged and measured on double-sided sticky tape (in preparation for the CT mount) (Figure 1). However, we determined that this can cause grains to sit in upright orientations, which is fine for CT scanning, but not for 2D measurements. For sample 97BS-CR8 each apatite grain was placed on a glass slide for 2D measurements and then transferred to the sticky tape for the CT mount to remedy this issue (Figure 1).
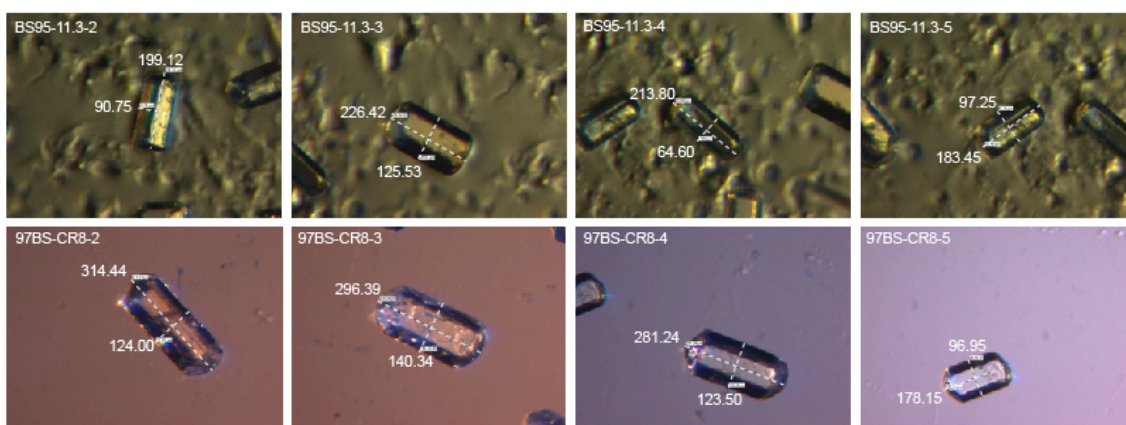
**Figure 1: Apatite grain photos with 2D measurements taken on an optical microscope. Dimensions are reported in µm and the grain aliquot name is in the top left corner of each photo. The top row is photographed on double sided sticky tape, and the bottom row is photographed on a glass slide.**

### 2.2 Grain mounting procedure for CT

Once the grains were measured optically in 2D, they were mounted for CT scanning by orienting several tens of grains on a plastic disc and stacking multiple discs (Figure 2). The procedure to create a single-layer mount for multi-grain scanning entails covering a flat top of a pushpin with double-sided sticky tape that can be pre-cut using a standard hole punch. Apatite grains are then picked directly onto the tape in a grid-like pattern. The pushpin surface is ~5 mm in diameter, which easily allows for ≥ 50 apatite grains to be mounted in one layer, tightly spaced, without touching. Grains could be

packed more densely as long as they can be reliably identified after scanning; they can even be touching, although this leads to a small increase in processing time to separate them using functions in the Blob3D software.

To utilize the total scanned volume, at least five multi-grain layers can be stacked for a single scan (up to 5 mm tall). To create stackable layers, sturdy plastic discs are made using a standard hole punch, with one side of the disc covered

5     with double-sided sticky tape and apatite grains mounted in the procedure outlined above. Once all the layers are mounted and all excess tape is trimmed, the discs are stacked on top of the push pin. The arrangement is secured by a thin wrap of parafilm. The parafilm and sticky tape are critical to ensure the crystals and layers do not move during scanning. This mount can be easily disassembled after scanning to retrieve the grains for further analysis.
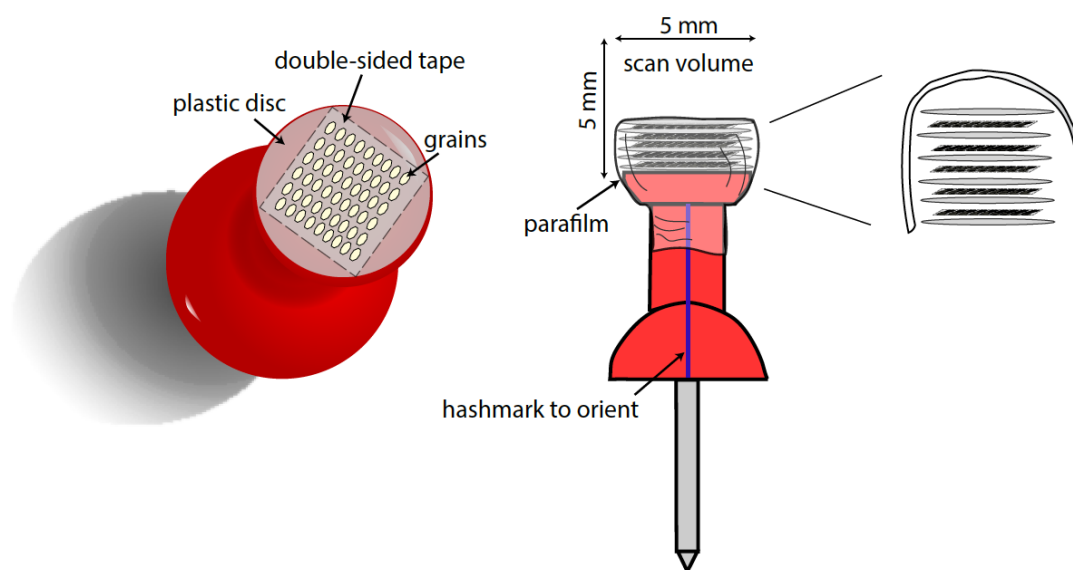
**Figure 2: Schematic rendering of CT mounting procedure. Grains are adhered to the top of a plastic disc using double sided sticky**
10    **tape, with multiple grains placed onto a 5x5 mm surface. Multiple plastic disk layers with grains may be assembled and then stacked to take full advantage of the height of the scan. These layers are held together using parafilm, and a hashmark on the pushpin enables further orientation of the scan in order to retrieve the grains afterwards for further analysis.**

### 2.3 X-ray CT Scanning

The multi-grain mounts were scanned with a Zeiss Xradia MicroXCT scanner at the University of Texas High-
15    Resolution X-ray CT Facility. Optimal scanning parameters will vary with the instrument being used, with top priorities being to minimize scanning artifacts and noise, while also minimizing time and cost. Lower X-ray energies are more sensitive to compositional variations, but more prone to beam-hardening artifacts. We experimented with various settings in this study. The grain mount for sample 97BS-CR8 was scanned with X-rays set at 100 kV and 10W, with a 1.0 mm $SiO_2$ filter. 1153 views were gathered at 1.5s per view, for an acquisition time of 28.9 minutes. Source-mount distance was 37.7
20    mm, and mount-detector distance was 12.8 mm. The 2048x2048 camera data were binned by 2, and the lower-energy X-

rays and weaker filtering necessitated application of a beam hardening correction during reconstruction. The reconstructed data had a voxel (3D pixel) size of 5.03 µm.

The grain mount for sample BS95-11.3 was scanned with X-rays set at 150 kV and 10 W with a 1.6 mm $CaF_2$ beam filter, acquiring 571 views at 1.5s per view, for an acquisition time of 14.3 minutes, not including calibration. Source-mount 5 distance was 37.7 mm, and mount-detector distance was 17.8 mm. The camera data were binned by 2, and no beam hardening correction was applied during reconstruction. The resulting data had a voxel size of 4.58 µm.
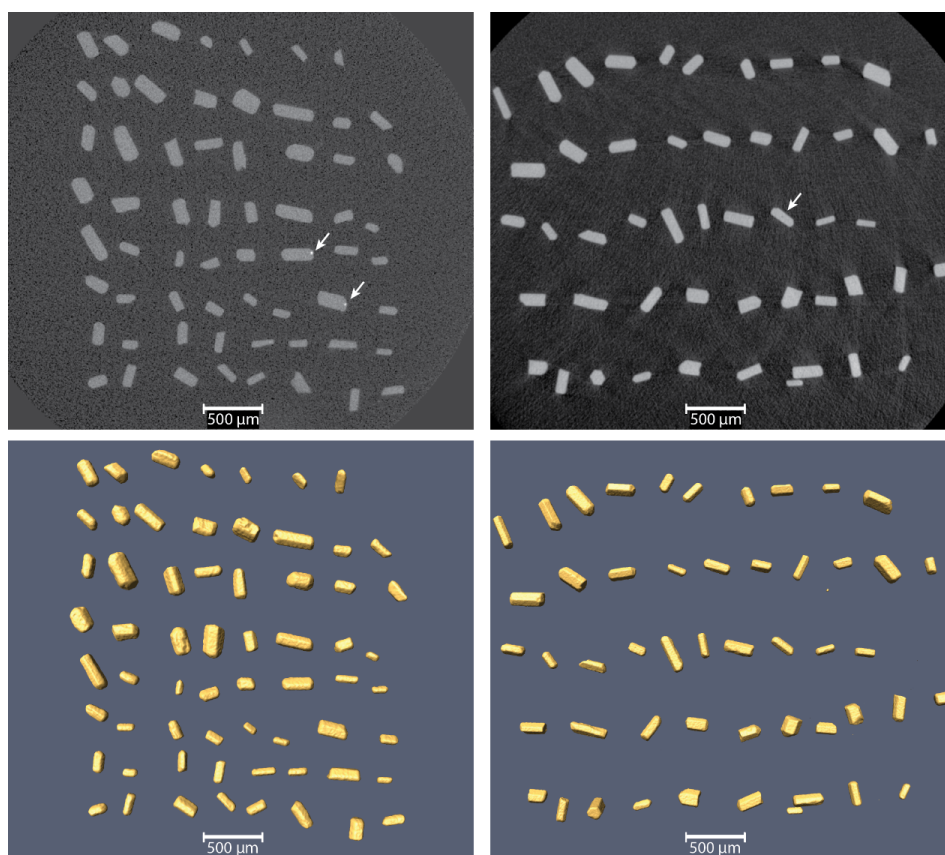
**Figure 3: Example CT slices (upper row) and 3D renderings (lower row) of apatite grain mounts for BS95 (left) and 97BS (right). Arrows indicate two grains with high-attenuation mineral inclusions in BS95, and a fluid inclusion in 97BS. CT slice for 97BS is**
10 **actually an oblique slice through the original data, to allow all grains to appear in the same image.**

Example images from the two data sets are shown in Figure 3, illustrating some of the trade-offs. The scan data for BS95 are noisier, due primarily to the faster acquisition, higher X-ray energy, and more severe filtering. Even with this level of noise, high-attenuation inclusions are evident. The scan data for 97BS are less noisy, allowing detection of a fluid inclusion, but beam hardening due to the lower-energy X-ray spectrum has caused faint streaks to emanate from or connect

some grains. These subtle artifacts have a negligible effect on measurements, but may be expected to increase in severity with more or higher-density grains. In both cases the 3D shapes are recovered well.

### 2.4 Grain size and shape, $F_T$, mass calculations

### 2.4.1 2D measurement calculations

5        The microscope length and width measurements are used to calculate volume and surface area, which are then used to calculate mass, ESR, and $UF_T$ and $ThF_T$ for each apatite grain, following methods laid out in Farley et al. (1996), Farley and Stockli (2002), and Farley (2002) (Figure 4). An equidimensional hexagonal prism geometry was assumed with the length (L) measurement for height of the prism, and the half-width (W) for the radius of the prism. All equations used for calculating these parameters are included below or in the Appendix.

EQ. 1 Volume (V):

$V = \frac{3 \times \sqrt{3}}{2} \times r^2 \times L$, where L is height and r is the half width.

EQ. 2 Surface Area (SA):

15   $SA = 6 \times r \times L + 3\sqrt{3} \times r^2$, where L is height and r is the half width

EQ. 3 Equivalent Spherical Radius (ESR):

$ESR = 3 \div \frac{SA}{V}$

20   EQ. 4 Mass:

$mass = 3.1(\frac{g}{cm^3}) \times V(mm^3) \times 1000$

EQ. 5 $UF_T$ and $ThF_T$ (2D case):

$UFt = 1 - \left(5.13 \times \frac{SA}{V}\right) + (6.78 \times \frac{SA^2}{V})$

25   $ThFt = 1 - \left(5.9 \times \frac{SA}{V}\right) + (8.99 \times \frac{SA^2}{V})$

EQ. 6 Mean $F_T$ (see Appendix for explanation)

   a)   From Farley et al., 1996 (used here for 2D calculations)

$F_T = a_{238} \times UF_T + (1 - a_{238}) \times ThF_T,$

where $a_{238} = (1.04 + 0.245 \times \frac{Th}{U})^{-1}$

b) From Blob3D, this study (used here for 3D calculations):

$$\overline{F_T} = A_{238}F_{T,238} + A_{232}F_{T,232} + (1 - A_{238} - A_{232})F_{T,235},$$

where $A_{238} = (1.04 + 0.247 \left[\frac{Th}{U}\right])^{-1}$ and $A_{232} = (1 + 4.21/ \left[\frac{Th}{U}\right])^{-1}$ 5

EQ. 7 Effective Uranium Concentration (eU) (see Appendix for explanation):

$$eU = [U] + 0.238[Th] + 0.0012[Sm]$$
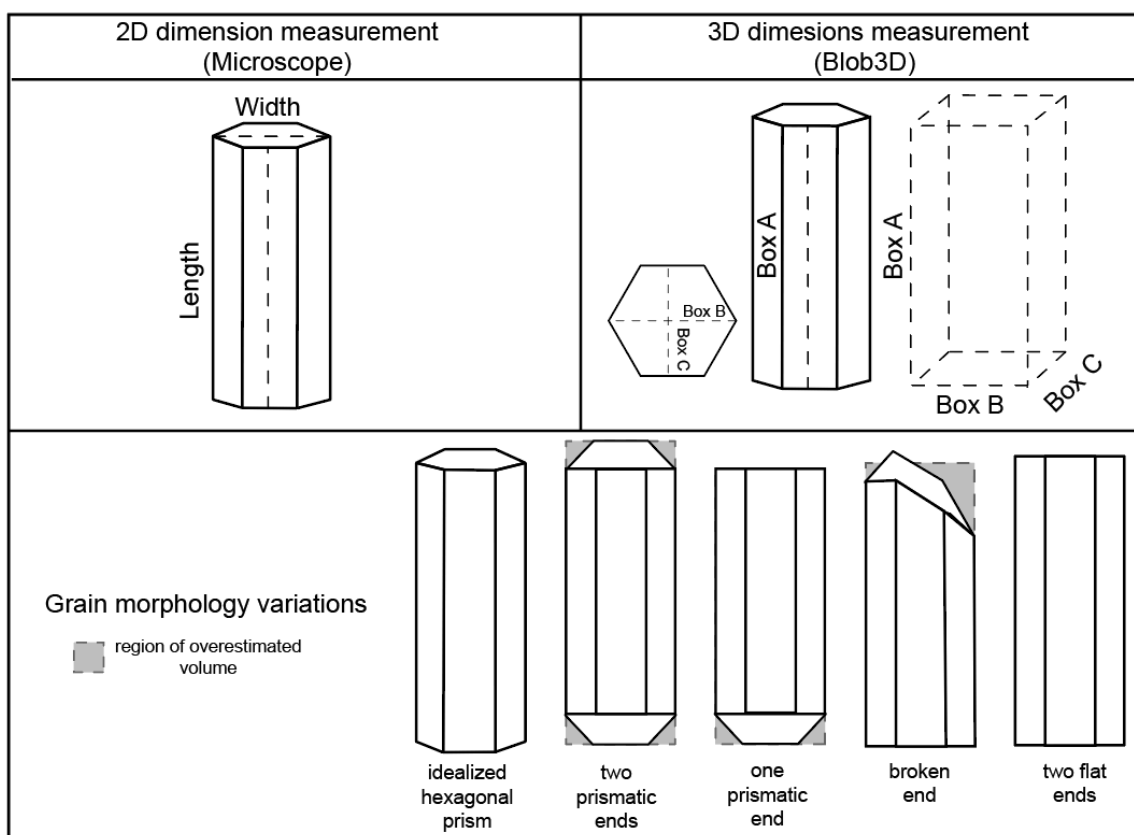
10 **Figure 4: (Top) Rendering of dimension data collected by 2D and 3D methods. Length and width are measured in 2D using an optical microscope measuring the long and wide axis of a grain. Blob3D reports the length, width and height (Box A, B and C) based on the best-fit rectangle for the grain dimensions. (Bottom) Rendering of the full range of variations in grain terminations**

**exhibited by the apatite in this study. Highlighted in gray are potential areas of over-estimated volume if an ideal hexagonal prism is assumed and calculated with 2D length and width data.**

**2.4.2 3D calculations**

Our principal 3D calculations were implemented in Blob3D (Ketcham 2005), a program written in the IDL

5 programming environment for efficient measurement of the dimensions, shape, and orientation of discrete features in volumetric data sets. The typical Blob3D method for calculating volume is to segment the grains based a threshold set at 50% of the CT number (grayscale) difference between apatite and the surrounding air. If grains are touching, or close enough to touching that their selected regions are connected, the software provides several separation methods, the simplest being an erode/dilate procedure. Volume is calculated as the number of voxels in a grain multiplied by the voxel volume,

10 and surface area is calculated by summing the areas of the triangular facets of an isosurface surrounding the grain, which is smoothed to reduce excess roughness from the cubic voxel edges. The shape parameters BoxA, BoxB, and BoxC are respectively the length (L), width (W), and height, corresponding to the dimensions of the smallest rectangular box that will enclose the grain (Ketcham and Mote, 2019). BoxC is calculated as the shortest 3D caliper length, BoxB is the shortest caliper length orthogonal to BoxC, and BoxA is the caliper length perpendicular to BoxC and BoxB (Figure 4).

15 A Monte Carlo method was implemented to measure $F_T$, probably similar in many, but not all, respects to previous work (Herman et al., 2007; Glotzbach et al., 2019). Stopping distances for $^{238}$U, $^{235}$U, $^{232}$Th, and $^{147}$Sm for the set of minerals reported in Ketcham et al. (2011) are included in the software. Taking the set of selected voxels for a grain, the origin point for each alpha particle is selected by first randomizing from which voxel to start, and then an (x,y,z) location within that voxel. The direction for each particle is obtained by sequentially stepping through a list of near-uniformly distributed

20 orientations calculated by starting with an octahedron and subdividing each triangular face four times until there are 1026 vertices, which are then scaled to lie on a unit sphere (Ketcham and Ryan, 2004). This approach provides slightly better precision than randomizing orientations, and 200,000 Monte Carlo samples are sufficient to get precision to within 0.1% in all tests reported below. Separate $F_T$ factors for each decay chain ($F_{T,238}$, $F_{T,235}$, $F_{T,232}$, $F_{T,147}$) are calculated, and a revised method for calculating mean $F_T$ that more precisely accounts for $^{235}$U is provided in EQ 6 (explanation in the Appendix).

25 If the resolution of the scan is low with respect to the stopping distance (stopping distance/voxel size > 4), excess surface roughness effects from voxelation are reduced by super-sampling. The voxels for each grain, and surrounding voxels, are subdivided into 27 ($3^3$) elements, and the super-sampled volume is smoothed with a 5-voxel-wide cubic kernel. The result is then thresholded using a value that maintains the original volume as closely as possible.

These methods were tested on ideal spheres and cylinders, with radii of 63 and 31.5 µm and the latter with an aspect

30 ratio of 4. At voxel sizes up to 8 and 4 µm for the respective radii, mean $F_{T,238}$ values averaged within 0.2% of the ideal-shape values for spheres; further doubling the voxel sizes raised the mean error to 0.5%. Cylinders performed better, with a mean error of 0.3% when voxel sizes were ¼ of the radius.

In their Monte Carlo $F_T$ implementation, Herman et al. (2007) report poor precision for small spheres when their centers are not centered in a voxel, with errors rising to several percent for a 40-µm radius sphere with 6.3-µm voxels across a range of center locations (calculated $F_T$ range ~0.58-0.67). Errors of this magnitude correspond to the effect of getting the radius wrong by plus or minus almost an entire voxel (~15% of the radius), too large to be reasonable and probably caused

5 by a problem with their test. We tested our segmentation method by running 100,000 trials randomizing the location of the sphere center using the same radius and voxel size and got maximum radius errors of +0.8/-1.1% and a standard deviation of 0.2%. We are thus confident that our implementation provides a high degree of accuracy and precision on even very small grains at low resolutions where voxel sizes are up to 25% of the radius.

We took three approaches to calculating ESR from the 3D data. The first two are based on the equivalent surface-

10 to-volume ratio (SV) approach (Meesters and Dunai, 2002). The model-based value $ESR_{SVm}$ uses the BoxA and BoxB caliper dimensions as L and W for equations (1) through (3), while the 3D CT-based value $ESR_{SV3D}$ uses the 3D-measured volume and surface area for equation (3). Because of the unsupported assumptions of the model approach and the shortcomings of surface area measurements, both discussed below, neither of these solutions are ideal. An alternative ESR is based on the equivalent-$F_T$ approach; Ketcham et al. (2011) demonstrated than an equivalent-$F_T$ sphere provides a more

15 accurate conversion for diffusion calculations than an equivalent-SV one. The set of calculations to determine the $F_T$-equivalent sphere radius $ESR_{FT}$ are provided in the Appendix.

### 2.5 (U-Th)/He procedure

The apatite (U-Th)/He ages were analyzed in the UTChron Thermochronology Laboratory at the University of Texas at Austin. Individual grains were measured, wrapped into platinum tubes, loaded into a 42-hole sample holder, and

20 pumped to ultra-high vacuum. Each aliquot was heated to ~1070°C for 5 minutes using a Fusions Diode laser system. The released gas was spiked with a $^3$He tracer, and purified by a Janis cryogenic cold trap at 40K and SAES NP-10 getter prior to measurement of the $^4$He/$^3$He on a Blazers Prisma QMS-200 quadrupole mass spectrometer. Final $^4$He contents were calculated using a manometrically-calibrated $^4$He standard of known concentration measured during the analytical run. All apatite aliquots were reheated once under the same conditions to ensure full gas release.

25 After degassing, the platinum packets containing the apatite grains were placed into plastic vials and dissolved in a 100 µl 30% $HNO_3$ $^{235}$U-$^{230}$Th-$^{149}$Sm spike solution for 90 minutes at 90°C. After acid digestion, 500 µl of Mili-Q ultra-pure $H_2O$ was added to dilute the solutions to ~5% $HNO_3$ and equilibrated for ≥ 24 hours prior to analysis. The solutions were analyzed using an Thermo Element2 HR-ICP-MS equipped with a 50µl/min micro-concentric nebulizer. Final $^{238}$U, $^{232}$Th, and $^{147}$Sm values were blank corrected and calibrated using a spiked, gravimetrically calibrated ~ 1 ppb standard solution.

30 Final (uncorrected) ages were calculated by solving the He age equation by means of Taylor Series expansion and reported with a 6% standard error, based on long-term intra-laboratory analysis of apatite age standards. Corrected final ages are determined by dividing the uncorrected age by the mean $F_T$ factor (EQ. 5). U, Th, and Sm concentration, although not used

in the age calculations, were determined for reporting purposes using the grain volumes and a nominal apatite density (e.g., Figure 4, EQ. 4).

## 3 Results

Blob3D provides 3D grain-specific volume, surface area, dimensions, and $F_T$ factors for each decay chain. The 2D

5  optical measurements provide dimension information, which are used to calculate volume, surface area, $UF_T$ and $ThF_T$ based on an assumed grain geometry of an equidimensional hexagonal prism (all results are reported in the appendix). We assume that the 3D-measured volume and $F_T$ values are accurate and serve to benchmark the 2D data (all comparisons reported in Table 1 and Figure 5). Surface area is more problematic to benchmark due to a number of factors, such as fractal roughness, CT data blurring and voxelation effects, as discussed below, and thus 2D and 3D results can only be compared in a relative

10  sense for surface area.

2D and 3D data are compared for each sample and as an entire population in Tables 1 and 2. The average 3D/2D ratio of each parameter is reported with its 1σ standard deviation. This average ratio shows whether the 2D measurements on average overestimates (ratio <1) or underestimates (ratio >1) the 3D measurements. Also reported is the absolute percent difference between the 2D and 3D measurements to illustrate the magnitude of deviation between the measurements.

15  While comparing 2D and 3D results, it became apparent that one 2D grain measurement was made at an incorrect microscope magnification setting, causing the length and width to be off by 2x, far greater than every other grain measured. Hence, this grain measurement (97BS-CR8-1) was not included when calculating the average differences between 3D and 2D measuring techniques.

### 3.1 Grain factors

20  Grains from both samples display a range of habits typical for apatite, including two flat ends, two prismatic ends, one flat and one prismatic end, and one or two broken or chipped ends (Figures 1 & 4). The grain morphology and the presence of any visible inclusions were recorded during handpicking (Table 2). Surprisingly, there are no clear systematic relationships between the presence of inclusions and grain age, or grain shape and ESR, volume, or surface area. The 2D length measurements are on average ~2% smaller than the 3D BoxA dimension. On the other hand, the 2D width dimension

25  is on average ~3% greater than the 3D BoxB dimension (Table 1).

One inevitable source of uncertainty in 2D length and width measurements is analyst judgment and error. For example, if a grain has uneven terminations, it is at the analyst's discretion to measure the longest axis or split the difference, whereas the CT analysis always reflect the longest axis. Similarly, CT scanning is also not subject to any user error introduced by measuring the apatite grain not lying on its widest face, or at an incorrect magnification. In our dataset, a

30  couple grains have very large deviations from the CT-derived volume, which may be caused by the microscope

magnification setting being slightly off during measuring. In contrast to grain 97BS-CR8-1, we cannot attribute this as the cause with full certainty so we do not exclude these grains.

### 3.2 Volume and Surface Area

Volumes and surface areas calculated using the 2D microscope dimensions both average ~20% larger than the 3D

5    calculations for both volumes and surface areas ($3D/2D_{VOL}$ = 0.82, $3D/2D_{SA}$ = 0.81) (Table 1, Figure 5). Specifically, 2D volumes and surface areas calculated from length and width data assuming a hexagonal prism shape have an absolute average difference of 23 ± 32% (2σ) and 22 ± 18% (2σ), respectively, from 3D Blob3D calculated volumes and surface areas.

### 3.3 ESR and Mass

10    The 2D ESR is calculated using the surface area to volume ratio (SA/V), which is derived assuming a hexagonal prism with the length and width dimensions measured on the microscope (EQ. 2, Figure 6). The 3D data had the ESR calculated based on SA/V in two ways. First, the SA/V for $ESR_{SVm}$ is calculated using the BoxA and BoxB values provided by Blob3D and assuming a hexagonal prism, mimicking the 2D approach. The variation between 2D and 3D $ESR_{SVm}$ measurements has a 2σ spread of ± 12%, but the variability is fairly evenly split in over- and under-estimating the ESR, such

15    that the average 3D/2D ratio is 1.02. Second, the 3D SA/V is calculated using the surface area and volume measurements output by Blob3D ($ESR_{SV3D}$). The variation between 2D and 3D $ESR_{SV3D}$ is even larger at ±18% (2σ), with an average 3D/2D ratio of 1.01 (Table 1, Figure 5).

The $F_T$-based ESR was on average similar to the SV-based one ($ESR_{FT}/ESR_{SVm}$ = 1.0), but the variation was ±9% for the two samples, and extreme values were 9% higher and 21% lower.  The relative variation of the $ESR_{FT}$ value with the

20    2D data is ±14%, similar to that for the other 3D ESR calculations (Table 1, Figure 5).

The grain mass is calculated from the volume data using a nominal apatite density, and therefore 2D and 3D mass determination directly reflect the variability in the 2D and 3D volume data. The 2D approach consistently overestimates the mass, with a high degree of scatter (3D/2D = 0.82 ± 0.44 (2σ)) (Table 1, Figure 5).

### 3.4 $F_T$ corrections

25    $UF_T$ and $ThF_T$ correction factors calculated from the 2D data are generally 1-2% lower than the Blob3D U and Th $F_T$ factors.  To combine the $F_T$ factors into a single term that is applied to the (U-Th)/He age, a mean $F_T$ was calculated in two ways using EQ. 6 (see methods). This results in mean $F_T$ factors that vary by an average of 2% between the 2D and 3D datasets. The 1σ scatter in 3D/2D FT factors is 1.8%, though individual differences can reach up to 9% (Table 1, Figure 5).

### 3.5 (U-Th)/He age and effective uranium

We calculated the apatite (U-Th)/He corrected age by dividing the raw (U-Th)/He age by the mean $F_T$ factor. The $2DF_T$ (U-Th)/He ages tend to be slightly older than the $3DF_T$ (U-Th)/He ages (3D/2D = 0.99), owing to the fact that the $2DF_T$ values are slightly lower (leading to a larger correction) (Table 1, Figure 5). The average difference between the 2D

5 and 3D $F_T$ corrected ages is 2%, mimicking that of the variation between 2D and 3D $F_T$. This has an insignificant impact on the mean age and uncertainty for both samples. Sample 97BS-CR8 has a $2DF_T$ mean age of 56.8 ± 2.9 Ma, and a $3DF_T$ mean age of 56.0 ± 2.9 Ma (Table 2, Figure 5). Sample BS95-11.3 has a $2DF_T$ age of 12.2 ± 4.0 Ma and a $3DF_T$ mean age of 12.1 ± 4.0 Ma (Table 2, Figure 5).

The effective uranium concentrations (eU = [U] + [Th]*0.238 + [Sm]*0.0012) for the apatite are normalized to the

10 mass of the grain. Since 2D and 3D grain masses calculations varied by ~25%, the eU concentration measurements vary by a similar degree (3D/2D = 1.29 ± 0.24 (2σ)) (Table 1, Figure 5). Note, not all grains were analysed for U, Th, and Sm and so there are less data for eU comparison than mass.
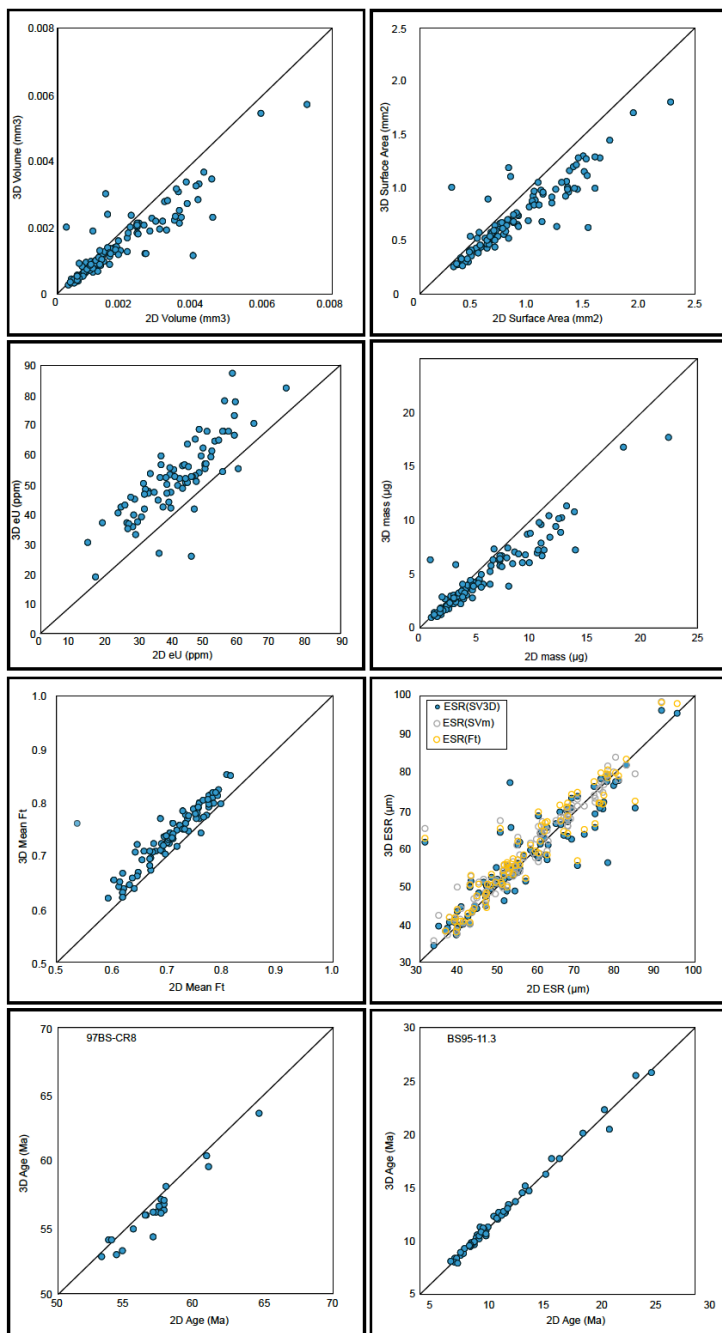
**Figure 5: XY plots for Volume, Surface Area, eU, Mass, Mean $F_T$, ESR, and Age for both samples. Both samples are plotted together, unless otherwise noted. Each data point represents a single apatite aliquot. Black lines represent 1:1. 3D data measurements plotted on Y-axis in all plots. 2D measurements overestimate volume, surface area and mass, and underestimate eU and mean $F_T$.**

## 4 Discussion

### 4.1 Accuracy of 2D vs 3D grain measurements

#### 4.1.1 Volume and surface area

One of the main motivations behind this study was to assess the accuracy of 2D grain measurements and using an
5     assumed grain geometry for calculating grain parameters (volume, ESR, mass, $F_T$) and the impact on the accuracy of the
final (U-Th)/He age and eU. For this reason, we selected two samples with relatively simple geologic histories, in order to
reduce the impact of geologic or kinetic factors that could lead to age dispersion.

The most striking deviations between 2D and 3D measurements is in the volume and surface area, which 2D
measurements consistently overestimated by 20-25% in our study, with a large degree of scatter ($1\sigma$ = 22% and 14%,
10     respectively). These results are in line with previous work. Evans and others (2008) observed a similar discrepancy in the 5
apatite grains they measured, where their 2D-based volumes were 30% greater than the 3D volumes (Table 3). Our dataset
contains >100 apatite grains, implying that the 2D overestimation of volume (and therefore mass) may be systematic in the
2D measurement approach. In contrast, Glotzbach and others (2019) analyzed 24 apatite grains and found that the 2D
volume measurements varied by a similar magnitude (~15%), but did not systematically overestimate the volume as in our
15     study and Evans et al (2008) (Table 3).  This is likely due in large part to their procedure of selecting the appropriate shape
model on a grain by grain basis, including ellipsoids for anhedral grains and accounting for terminations using the functions
provided in Ketcham et al. (2011), rather than assuming exclusively flat-terminated hexagonal prisms.

There are multiple factors that can contribute to overestimating the volume of a given apatite crystal. First, the
assumption of a hexagonal prism crystal shape with flat terminations, in which the length of the grain is used as the height of
20     the prism, has the potential to overestimate the volume if the crystal has tapered ends (Figure 4). However, our data suggest
this can only account for about a third of the volume difference, because even crystals with two flat (or broken) ends still had
an average volume difference of 13%. Second, the ideal-prism model also presumes a perfect, equal-sided hexagonal cross
section perpendicular to the c-axis, for which the ratio of width to height should be 2/sqrt(3), or 1.1547.  The 3D shape
measurements give mean ratios of 1.25(02) and 1.23(01) for our two samples, indicating that the cross sections are on
25     average flatter than ideal hexagonal prisms.  The non-ideality of this cross section was also noted by Glotzbach et al. (2019),
and can result in either an underestimate or overestimate of volume, depending on which face the grain is lying on when
measured in 2D.  The systematic bias we observe is not surprising as apatite commonly come to rest on their flatter side,
whereas some of our observed scatter comes from this not always being the case. This shape divergence explains about a
quarter of the departure between 2D and 3D volume in our data. The remaining deviation may be due to chipped crystals,
30     surface roughness, or other deviations from a perfect prism that the 2D calculation cannot account for.

A number of factors will directly impact surface area calculations. Surface area is calculated from the 2D
measurements by assuming a perfectly smooth prism. CT has the potential to capture irregular surfaces present in natural
apatite grains, which if present and resolution is sufficient, should lead to higher surface area calculations in the 3D data.

However, surface area is problematic to measure, regardless of resolution. Irregular surfaces are to some degree fractal entities, making their measured areas dependent on measurement scale, and the "correct" answer is not straightforward to define. All CT images are naturally blurry to some extent, smoothing out both irregularities and also sharp corners and edges. Conversely, the 3D measurement process of segmentation by thresholding can lead to artificial enhancement of

5   surface area due to "voxelation" effects (the 3D equivalent of pixilation).

In our data, the 2D measurements consistently result in a higher surface area than the 3D measurements. This is probably partly due to the ~5-µm resolution of our CT data, and also to the flat-terminated hexagonal prism model leading to an overestimate. Evans et al. (2008) observe a similar discrepancy in surface area measurements between 2D and 3D data (2D ~23% higher) with a 3.77 µm resolution scan (Table 3). On the other hand, Glotzbach et al., (2019) scanned their grains

10   at a 1.2 µm resolution and their 2D measurements gave surface areas on average 8% lower than 3D (Table 3). As with volume, a large part of the difference is probably due to using a more accurate shape model than an ideal equal-sided hexagonal prism. The overshoot may be in part due to their higher CT data resolution capturing roughness better, but their 3D images also show voxelation effects such as ridge sets on flat surfaces that likely increased their surface areas to an unknown extent.

15   **4.1.2 Mass and eU**

The discrepancy in volume between 2D and 3D measurements directly impacts the mass calculation, causing the grain masses derived from the 2D measurements to be ~25% higher than the 3D grain mass determinations (Figure 6). Evans and others (2008) found similar deviations, with their masses calculated from 2D volumes ~30% greater than their masses for 3D volumes (Table 3). Both of these divergences stem from using the assumption of a flat-ended hexagonal prism,

20   whereas an approach that takes grain shape into account when choosing the $F_T$ formula (Ketcham et al., 2011; Glotzbach et al., 2019) avoids this systematic bias. However, in all cases that use perfect shape models, the relative scatter is on the order of 20% (1σ), which is high enough to be worth fixing.

Although the age equation does not require knowledge of the grain volume or mass, both are necessary to calculate reported concentrations for U, Th, Sm and He (Figure 6). The U, Th, Sm concentrations, often combined into a single term,

25   'effective uranium' (eU), has been used a proxy for radiation damage within a crystal, and age versus eU correlations are commonly used for interpretation of age scatter, and thermal history inverse modeling (e.g., Flowers et al., 2009; Guenthner et al., 2013). Therefore, accurate knowledge of volume has cascading effects from mass to eU concentration and age interpretation (Figure 6). Comparison between eU calculated for the 3D mass data and 2D mass data show that the 2D masses underestimate the bulk eU concentrations by ~20-30%. This is consistent with the 2D mass data being ~25% higher

30   than the 3D mass data, which would have the effect of 'diluting' the eU signal.

### 4.1.3 ESR

The various ESR calculations all yielded similar results on average, but high degrees of variation between measurement and calculation modes (5-6%). In addition to being more accurate for simplifying complex shapes to spheres for diffusion calculations, the $ESR_{FT}$ method is also likely more robust than others that presume or measure surface area.

5 Surface area, beyond being difficult to define and measure for irregular natural objects in a resolution-resistant way, has only secondary importance for diffusion and $F_T$ calculations when it varies on a fine scale compared to the grain (i.e. µm-scale roughness).

### 4.1.4 $F_T$

A somewhat surprising result of our study is that, despite volume and surface areas being very different between the

10 2D and 3D methods, these differences largely cancelled each other out in S/V-based $F_T$ calculations. This is in large part because volume and surface area co-vary, both in the assumed models and the actual measurements, so an error in one leads to a similar-magnitude error in the other (Figure 6).

A result that more closely conformed to expectation is that, as grain size fell, dispersion between 2D and 3D $F_T$ values increased, although it remained modest. The standard deviation of 3D/2D $U_{FT}$ was 2.7% for grains with $U_{FT}$ values

15 from 0.6-0.7, 2.4% from 0.7-0.8, and 1.3% for grains above 0.8.
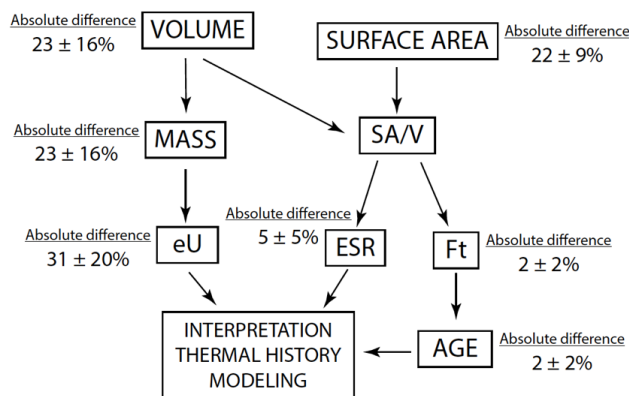
**Figure 6: Workflow diagram showing the effect of volume and surface area measurements on other parameters used for (U-Th)/He age calculation and interpretation. The average absolute difference between 2D and 3D measurements for each of the parameters are reported with their 1σ uncertainties (reported in Table 1). Note the greatest deviations are in volume and surface**

20 **area, and those parameters that rely on volume alone. ESR, $F_T$ and age deviate less because they use the SA/V, which is ~1 between 2D and 3D measurements.**

### 4.2 Reproducibility of (U-Th)/He ages

In addition to assessing the accuracy of using the 2D measurements, this study aimed to quantify the uncertainties that may be introduced by such measurements, particularly in $F_T$, as a means to potentially improve age accuracy, precision, and intra-sample dispersion. Previous studies have estimated that uncertainties in $F_T$ calculation can account for 1-5% of

5   sample age uncertainty (Evans et al., 2008; Glotzbach et al., 2019). Our results are consistent with this range, and suggest that uncertainties in the U and Th $F_T$ calculation are on the order of 1-3%, and mean $F_T$ varies by 2%. We find the greatest deviations are caused by user error and not the assumed grain geometry. In samples with less euhedral apatite grains, the effects of $F_T$ and an assumed grain geometry can increase.

Our data also show that the 3D $F_T$ correction does not increase the overall sample age precision. For sample 97BS-

10  CR8, 24 apatite grains were analyzed, two of which are outliers. Of the two outliers, one (97BS-CR8-1) was clearly caused by a user error during microscope measurement, leading to an incorrect $F_T$ correction (0.55) and old age (78.8 Ma). This was discovered during 3D image processing, in which the same grain was identified, measured correctly, and produced an $F_T$ of 0.76 and a more congruent corrected age of 57.2 Ma. In contrast, for a second outlier (97BS-CR8-24), the 2D and 3D $F_T$ corrected ages both produced anomalous ages of 101.2 and 98.4 Ma, respectively. An unusually high He concentration the

15  likely culprit for the old age for this grain, potentially due to He implantation, but the reason for the high He concentration is not evident from our data. Excluding these two outliers, the average age and uncertainty for the sample population (n=22 grains) calculated based on the 2D and 3D measurements are indistinguishable (56.8 ± 2.9 Ma and 56.0 ± 2.9 Ma); relative errors are 5.1% in both cases.

Similarly, the sample ages calculated with 3D and 2D data for 95BS-11.3 (n=59 aliquots) are indistinguishable,

20  12.2 ± 4.0 and 12.1 ± 4.0 Ma, respectively. Unlike sample 97BS-CR8, there was no clear-cut evidence of user error, and the relatively high age uncertainty (33%) is reproducible between the 2D and 3D$F_T$ corrected ages. Five aliquots produced ages > 20 Ma, which skews the mean age older (the median age is 10.2 Ma, within error of the previous reported age in Stockli et al., 2002). The apatite ages do not correlate with factors such as ESR (grain size) or eU. The >20 Ma aliquots all have high He concentrations (nmol/g) compared with the bulk of the sample, suggesting that excess He, possibly due to implantation

25  from high U-Th neighbors, or the presence of undetected and insoluble high-eU inclusions.

Overall, these data suggest that although the 3D$F_T$ can provide a more accurate $F_T$ correction and varies from 2D estimations by ~2%, it has a minimal effect on the calculated sample age (1-2%) and no effect on the reproducibility for these two samples. This is not surprising, as a ~2% error would constitute a negligible proportion of the often cited 6% dispersion derived from analyzing age standards; error propagation indicates that removing a source of 2% error would only

30  reduce an overall 6% error to 5.7%. This points to the importance of other factors in intra-sample dispersion, such as U-Th zonation, and/or excess He from nano-inclusions or high U-Th neighbors.

### 4.3 Effects of inclusions or broken grains

It is widely regarded that inclusions and broken grains are both contributors to intra-sample dispersion and inaccurate He ages, particularly anomalously old ages. Inclusions in apatite can act as He traps or a source for excess He, particularly mineral inclusions that do not dissolve during apatite $HNO_3$ digestion. Both apatite samples had multiple grains
5    with high density and low density inclusions detectable by microscope during picking and/or the CT scan. In both samples, the presence of inclusions did not have any discernable effect on the (U-Th)/He age. While inclusions are almost certainly a source for error and dispersion in some samples, at least the easily visible one do not appear be relevant in these samples, which suggests they are likely also not U-Th bearing inclusions.

Similarly, broken grains can be a source of dispersion if they were broken after the sample passed through the He
10  partial retention zone, e.g., after the grain began to accumulate He (see Brown et al., 2013a). Typically, this may occur during erosional transport or during mineral separations. Brown and others (2013) assess that broken grains can contribute from 7 to > 50% dispersion from the sample age, depending on cooling history. In our samples, grain terminations varied from doubly prismatic to flat, and in some cases appeared chipped or broken. However, there is no clear correlation between the chipped or broken grains and He age. One possibility is that the grains broke prior to cooling through the He retention
15  zone. This seems somewhat unlikely, given that both samples come from crystalline rocks. Alternatively, and perhaps more plausibly, the variety of crystal habits may reflect how the crystals grew in the host rock. In any case, the grains in these samples that appear to be chipped or broken are not obvious sources for the age dispersion observed in the samples.

### 4.4 Benefits and limitations of X-ray CT over microscope measurements

CT scanning mineral grains for (U-Th)/He chronometry has both analytical and practical benefits. CT provides
20  more accurate grain volume measurements, which becomes increasingly important as grain shapes deviate from idealized forms (e.g., abraded or broken grains). CT data are able to highlight inclusions or other internal heterogeneities based on contrasts in density in the X-ray data, which may not be visible by the naked eye. Furthermore, the CT-mounting method outlined in this study allows for the scanning of up to 250 grains in a single session, and potentially many more, making it cost and time effective. Different mineral phases can be scanned together, and data can be processed in a batch so that from a
25  single scan, one can gather volume, surface area, caliper dimensions, $F_T$, mass, and ESR at once for several samples and phases. We anticipate that more volume-based shape measurements can and will be developed to automatically and quantitatively evaluate grains for euhedrality, rounding, broken faces, and a wealth of other potentially informative data.

CT scanning mineral grains used for (U-Th)/He dating also has the benefit of removing the possibility of 'user error' during the grain measurement step. Unlike with microscope measurements, the orientation of the apatite grain on the
30  CT mount does not matter, and there is no need to set a magnification or trace the dimensions of the grain by hand, reducing potential for mistakes. CT also eliminates variability that may arise from different microscopes, lighting conditions, and

imaging software, and creates a digital archive of 3D grain shapes, densities and internal structures that a microscope photo cannot capture.

The main limitation of using CT is access to the instrumentation and cost for sample analysis. However, CT scanners are becoming more common as desktop instruments in earth science departments, and many universities have
5   imaging facilities that include micro-CT machines. As CT instruments continue to proliferate and costs continue to fall, we anticipate that measuring, screening, and documenting grains used for thermo-geochronology will become a widely-used practice.

**5 Conclusions**

The shape and size of 109 apatite grains from two rapidly-cooled plutonic samples were analysed by 2D and 3D
10   methods. 2D length and width measurements made on an optical microscope were used to calculate surface area, volume, ESR, mass, $F_T$ and eU, assuming an ideal equal-sided hexagonal prism grain shape. The same apatite crystals were scanned using x-ray computed tomography at a 4-5 μm resolution, and the same factors were calculated using Blob3D software, which does not require assuming a grain shape. 83 new apatite (U-Th)/He ages were collected to resolve the influence of 2D versus 3D $F_T$ correction factors on final (U-Th)/He age and reproducibility. With these data, we derive the following
15   conclusions:

1.   Deviations between 2D and 3D measurements were greatest in volume and surface area (~25%), which caused mass and eU calculations to deviate by a similar magnitude. Volume and surface area measurements also showed high dispersion of 16% and 9%, respectively.

2.   2D $F_T$ measurements only contribute ~ 2% error on average, even with the erroneous assumption of an ideal grain
20   shape.

3.   Inclusions and broken or chipped ends did not have a discernible impact on the (U-Th)/He age dispersion in these samples.

4.   The combined (U-Th)/He ages for each sample were indistinguishable for 2D and 3D $F_T$ corrections. Similarly, the amount of intra-sample dispersion was identical (both >5%). This implies that factors other than $F_T$ dominate the
25   intra-sample uncertainty.

In addition, we present a bulk scanning method that easily allows analysis of > 250 grains in a single session, and new Blob3D software 3D $F_T$ and $ESR_{FT}$ functions.

**Acknowledgements**

We thank Jessie Maisano for acquiring and reconstructing the CT data. These data were collected at the UTCT NSF Multi-User Facility. This work was funded through Jackson School of Geosciences funds to Stockli and UTCT facility support (EAR-1762458) to Ketcham, and an NSF GRF and WHOI Postdoc Scholarship to Cooperdock.

5 **References**

Bargnesi, E.A., Stockli, D.F., Hourigan, J.K., Hager, C., 2016. Improved accuracy of zircon ( U – Th )/ He ages by rectifying parent nuclide zonation with practical methods. Chem. Geol. 426, 158–169. https://doi.org/10.1016/j.chemgeo.2016.01.017

Evans, N.J., McInnes, B.I.A., Squelch, A.P., Austin, P.J., McDonald, B.J., Wu, Q., 2008. Application of X-ray micro-
10 computed tomography in (U-Th)/He thermochronology. Chem. Geol. 257, 101–113. https://doi.org/10.1016/j.chemgeo.2008.08.021

Farley, K.A., 2002. (U-Th)/He Dating: Techniques, Calibrations, and Applications. Rev. Mineral. Geochemistry 47, 819–844. https://doi.org/10.2138/rmg.2002.47.18

Farley, K.A., Stockli, D.F., 2002. ( U-Th )/ He Dating of Phosphates: Apatite, Monazite, and Xenotime. Rev. Mineral. Geochemistry 15, 559–577. https://doi.org/10.2138/rmg.2002.48.15

Farley, K.A., Wolf, R.A., Silver, L.T., 1996. The effects of long alpha-stopping distances on (U - Th)/He ages. Geochim.
20 Cosmochim. Acta 60, 4223–4229. https://doi.org/http://dx.doi.org/10.1016/S0016-7037(96)00193-7

Flowers, R.M., Ketcham, R.A., Shuster, D.L., Farley, K.A., 2009. Apatite (U-Th)/He thermochronometry using a radiation damage accumulation and annealing model. Geochim. Cosmochim. Acta 73, 2347–2365. https://doi.org/10.1016/j.gca.2009.01.015

Gautheron, C., Tassan-Got, L., Ketcham, R.A., Dobson, K.J., 2012. Accounting for long alpha-particle stopping distances in (U-Th-Sm)/He geochronology: 3D modeling of diffusion, zoning, implantation, and abrasion. Geochim. Cosmochim. Acta 96, 44–56. https://doi.org/10.1016/j.gca.2012.08.016

30 Glotzbach, C., Lang, K.A., Avdievitch, N.N., Ehlers, T.A., 2019. Increasing the accuracy of (U-Th(-Sm))/He dating with 3D grain modelling. Chem. Geol. 506, 113–125. https://doi.org/10.1016/j.chemgeo.2018.12.032

Guenthner, W.R., Reiners, P.W., Ketcham, R.A., Nasdala, L., Giester, G., 2013. Helium diffusion in natural zircon: radiation damage, anisotropy, and the interpretation of zircon (U-TH)/He thermochronology. Am. J. Sci. 313, 145–198. https://doi.org/10.2475/03.2013.01

5  Herman, F., Braun, J., Senden, T.J., Dunlap, W.J., 2007. (U-Th)/He thermochronometry: Mapping 3D geometry using micro-X-ray tomography and solving the associated production-diffusion equation. Chem. Geol. 242, 126–136. https://doi.org/10.1016/j.chemgeo.2007.03.009

Hourigan, J.K., Reiners, P.W., Brandon, M.T., 2005. U-Th zonation-dependent alpha-ejection in (U-Th)/He chronometry.
10  Geochim. Cosmochim. Acta 69, 3349–3365. https://doi.org/10.1016/j.gca.2005.01.024

Ketcham, R.A., 2005.  Computational methods for quantitative analysis of three-dimensional features in geological specimens. Geosphere, 1(1), 32-41.  https://10.1130/GES00001.1

15  Ketcham, R.A., Gautheron, C., Tassan-Got, L., 2011. Accounting for long alpha-particle stopping distances in (U-Th-Sm)/He geochronology: Refinement of the baseline case. Geochim. Cosmochim. Acta 75, 7779–7791. https://doi.org/10.1016/j.gca.2011.10.011

Ketcham, R.A., Mote, A.S., 2019. Accurate measurement of small features in X-ray CT data volumes, demonstrated using
20  gold grains.  Journal of Geophysical Research, 124.  https://10.1029/2018JB017083

Ketcham, R.A., Ryan, T.M., 2004.  Quantification and visualization of anisotropy in trabecular bone.  Journal of Microscopy, 213, 158-171.  DOI: 10.1111/j.1365-2818.2004.01277.x.

25  Stockli, D.F., Surpless, B.E., Dumitru, T.A., Farley, K.A., 2002. Thermochronological constraints on the timing and magnitude of Miocene and Pliocene extension in the central Wassuk Range, western Nevada. Tectonics 21. https://doi.org/10.1029/2001TC001295

Surpless, B., Stockli, D.F., Dumitru, T.A., Miller, E.L., 2002. Two-phase westward encroachment of Basin and range
30  extension into the northern Sierra Nevada. Tectonics 21, 2-1-2–13. https://doi.org/10.1029/2000TC001257

**Table 1: Comparison of 2D and 3D measurement data**

| Sample | n (grains) | Avg 3D/2D | 1σ | Absolute Difference | | | | |
|---|---|---|---|---|---|---|---|---|
| | | | | Avg | 1 σ | Median | Max | Min |
| **LENGTH** | | | | | | | | |
| 97BS-CR8 | *49* | 1.00 | 0.03 | 2 | 2 | 2 | 7 | 0.1 |
| BS95-11.3 | *59* | 0.97 | 0.1 | 6 | 7 | 5 | 49 | 0.1 |
| Combined | *108* | 0.98 | 0.1 | 4 | 6 | 3 | 49 | 0.1 |
| **WIDTH** | | | | | | | | |
| 97BS-CR8 | *49* | 1.04 | 0.05 | 15 | 8 | 14 | 32 | 0.2 |
| BS95-11.3 | *59* | 1.03 | 0.09 | 17 | 9 | 17 | 44 | 1 |
| Combined | *108* | 1.03 | 0.07 | 16 | 8 | 16 | 44 | 0.2 |
| **VOLUME** | | | | | | | | |
| 97BS-CR8 | *49* | 0.85 | 0.25 | 22 | 19 | 18 | 109 | 2 |
| BS95-11.3 | *59* | 0.80 | 0.20 | 24 | 14 | 23 | 80 | 5 |
| Combined | *108* | 0.82 | 0.22 | 23 | 16 | 20 | 109 | 2 |
| **SURFACE AREA** | | | | | | | | |
| 97BS-CR8 | *49* | 0.83 | 0.15 | 21 | 10 | 20 | 60 | 4 |
| BS95-11.3 | *59* | 0.80 | 0.12 | 22 | 8 | 21 | 43 | 3 |
| Combined | *108* | 0.81 | 0.14 | 22 | 9 | 20 | 60 | 3 |
| **MASS** | | | | | | | | |
| 97BS-CR8 | *49* | 0.85 | 0.25 | 22 | 19 | 18 | 109 | 2 |
| BS95-11.3 | *59* | 0.80 | 0.20 | 24 | 14 | 23 | 80 | 5 |
| Combined | *108* | 0.82 | 0.22 | 23 | 16 | 20 | 109 | 2 |
| **ESR ($SV_m$)** | | | | | | | | |
| 97BS-CR8 | *49* | 1.03 | 0.04 | 4 | 4 | 2 | 21 | 0.1 |
| BS95-11.3 | *59* | 1.02 | 0.08 | 5 | 6 | 4 | 32 | 0.03 |
| Combined | *108* | 1.02 | 0.06 | 5 | 5 | 3 | 32 | 0.03 |
| **ESR ($SV_{3D}$)** | | | | | | | | |
| 97BS-CR8 | *49* | 1.01 | 0.10 | 6 | 8 | 3 | 45 | 0.04 |
| BS95-11.3 | *59* | 1.00 | 0.08 | 6 | 5 | 4 | 26 | 0.02 |
| Combined | *108* | 1.01 | 0.09 | 6 | 7 | 4 | 45 | 0.02 |
| **ESR ($F_T$)** | | | | | | | | |
| 97BS-CR8 | *49* | 1.03 | 0.04 | 4 | 3 | 4 | 12 | 1 |
| BS95-11.3 | *59* | 1.02 | 0.08 | 6 | 6 σ | 5 | 28 | 0.1 |
| Combined | *108* | 1.02 | 0.07 | 5 | 5 | 4 | 28 | 0.1 |

| | | | | | | | | |
|---|---|---|---|---|---|---|---|---|
| **U F$_T$** | | | | | | | | |
| 97BS-CR8 | *49* | 1.02 | 0.02 | 2 | 1 | 2 | 8 | 0.1 |
| BS95-11.3 | *59* | 1.01 | 0.03 | 2 | 2 | 2 | 9 | 0.1 |
| Combined | *108* | 1.01 | 0.02 | 2 | 2 | 2 | 9 | 0.1 |
| **TH F$_T$** | | | | | | | | |
| 97BS-CR8 | *49* | 1.01 | 0.02 | 2 | 1 | 1 | 7 | 0.01 |
| BS95-11.3 | *59* | 1.00 | 0.03 | 2 | 2 | 2 | 9 | 0.1 |
| Combined | *108* | 1.00 | 0.03 | 2 | 2 | 1 | 9 | 0.01 |
| **MEAN F$_T$** | | | | | | | | |
| 97BS-CR8 | *49* | 1.02 | 0.02 | 2 | 1 | 1 | 5 | 0.2 |
| BS95-11.3 | *59* | 1.01 | 0.03 | 2 | 2 | 2 | 9 | 0.01 |
| Combined | *108* | 1.01 | 0.02 | 2 | 2 | 2 | 9 | 0.01 |
| **eU** | | | | | | | | |
| 97BS-CR8 | *49* | 1.24 | 0.12 | 24 | 12 | 22 | 49 | 3 |
| BS95-11.3 | *59* | 1.30 | 0.27 | 33 | 23 | 28 | 112 | 6 |
| Combined | *108* | 1.29 | 0.24 | 31 | 20 | 26 | 112 | 3 |
| **AGE** | | | | | | | | |
| 97BS-CR8 | *49* | 0.99 | 0.01 | 2 | 1 | 1 | 5 | 0.2 |
| BS95-11.3 | *59* | 0.99 | 0.03 | 2 | 2 | 2 | 8 | 0.01 |
| Combined | *108* | 0.99 | 0.02 | 2 | 2 | 2 | 8 | 0.01 |
| ESR(SVm) = BoxA and BoxB assuming hexagonal prism shape, ESR(SV3D) = Blob3D vol and SA measurements, ESR(Ft) = Ft equivalent sphere | | | | | | | | |

**Table 2: (U-Th)/He Age results**

| Aliquot | Grain morph. | 3DFt Age (Ma) | 2DFt Age (Ma) |
|---|---|---|---|
| **Sample 97BS-CR8-** | | | |
| *1* | *FL PR* | 57.2 | 78.8 |
| *2* | PR CH, i | 56.3 | 57.7 |
| *3* | PR PR | 54.1 | 53.8 |
| *4* | PR PR | 56.2 | 57.2 |
| *5* | PR PR | 58.0 | 57.9 |
| *6* | PR PR | 54.1 | 53.9 |
| *7* | PR PR | 60.3 | 60.8 |
| *8* | FL PR | 53.0 | 54.3 |
| *9* | FL PR | 57.1 | 57.5 |
| *10* | PR PR | 56.0 | 56.4 |
| *11* | FL FL, i | 54.9 | 55.5 |
| *12* | FL PR | 63.5 | 64.6 |
| *13* | FL PR | 56.7 | 57.7 |
| *14* | PR PR | 55.9 | 56.4 |
| *15* | PR PR | 56.6 | 57.4 |
| *16* | FL FL | - | - |
| *17* | FL PR | 57.0 | 57.8 |
| *18* | FL CH | - | - |
| *19* | FL PR | 52.8 | 53.2 |
| *20* | PR CH | 49.7 | 51.2 |
| *21* | PR CH | 59.5 | 60.9 |
| *22* | PR PR | 53.3 | 54.7 |
| *23* | PR CH | 56.2 | 57.0 |
| *24* | *PR PR* | 101.2 | 98.4 |
| *25* | PR PR | 56.1 | 57.5 |
| *26* | PR PR | 54.3 | 57.0 |
| *Average* | | **56.0** | **56.8** |
| *Stdev* | | **2.9** | **2.9** |
| *%RSD* | | **5.1** | **5.1** |
| **Sample BS95-11.3-** | | | |

| 1  | PR PR    | 10.5 | 10.3 |
|----|----------|------|------|
| 2  | FL PR    | 13.6 | 13.8 |
| 3  | FL PR    | 8.6  | 8.8  |
| 4  | PR PR    | 13.3 | 13.2 |
| 5  | FL PR    | 12.6 | 12.8 |
| 6  | PR PR    | 10.8 | 11.1 |
| 7  | PR PR    | 10.6 | 10.7 |
| 8  | FL PR    | 10.2 | 10.2 |
| 9  | PR PR    | 25.5 | 24.7 |
| 10 | PR PR    | 12.3 | 11.8 |
| 11 | PR CH    | 10.4 | 11.1 |
| 14 | FL PR    | 10.8 | 10.8 |
| 15 | FL PR    | 9.5  | 10.0 |
| 16 | FL PR    | 9.7  | 9.9  |
| 17 | FL CH    | 8.7  | 9.1  |
| 18 | PR CH    | 9.2  | 9.2  |
| 19 | FL PR    | 9.4  | 9.6  |
| 20 | FL FL    | 25.7 | 26.1 |
| 21 | FL PR    | 8.8  | 8.8  |
| 22 | PR PR    | 8.3  | 8.2  |
| 23 | PR CH, i | 12.6 | 12.2 |
| 24 | FL PR    | 10.8 | 10.9 |
| 25 | FL PR    | 9.8  | 10.0 |
| 26 | FL FL    | 10.1 | 10.5 |
| 27 | FL CH    | 15.1 | 14.7 |
| 28 | FL CH, i | 8.2  | 8.4  |
| 29 | PR CH    | 10.8 | 10.8 |
| 30 | PR PR, i | 12.5 | 12.8 |
| 31 | PR PR    | 12.0 | 12.1 |
| 32 | FL PR    | 14.6 | 15.0 |
| 33 | PR PR    | 17.6 | 17.1 |
| 34 | PR CH    | 11.0 | 10.9 |
| 35 | PR PR    | 12.1 | 12.1 |
| 36 | PR CH, i | 9.5  | 9.7  |
| 37 | FL FL    | 10.4 | 10.5 |

| 38 | FL CH | 9.6 | 9.8 |
|---|---|---|---|
| 39 | PR PR, i | 12.3 | 12.5 |
| 40 | PR PR | 7.9 | 8.3 |
| 41 | PR CH | 22.3 | 21.8 |
| 42 | PR PR | 11.2 | 11.3 |
| 43 | FL CH | 9.9 | 10.0 |
| 44 | PR PR | 9.7 | 9.8 |
| 45 | FL CH | 8.0 | 7.9 |
| 46 | PR PR | 11.0 | 11.0 |
| 48 | PR PR | 20.0 | 19.9 |
| 49 | PR CH, i | 17.6 | 17.8 |
| 50 | PR PR, i | 11.2 | 10.6 |
| 51 | FL PR, i | 14.5 | 14.4 |
| 52 | FL CH | 12.7 | 12.7 |
| 53 | FL PR | 12.9 | 13.0 |
| 54 | PR CH | 9.8 | 10.0 |
| 55 | PR PR | 9.6 | 9.6 |
| 56 | FL CH | 16.1 | 16.6 |
| 57 | PR PR | 11.1 | 10.8 |
| 58 | PR CH, i | 9.5 | 9.6 |
| 59 | PR PR | 20.4 | 22.3 |
| 60 | PR PR | 7.8 | 8.5 |
| 61 | FL CH | 10.8 | 10.7 |
| 62 | CH CH | 10.6 | 11.1 |
| *Average* | | **12.1** | **12.2** |
| *Stdev* | | **4.0** | **4.0** |
| *%RSD* | | **33.2** | **32.8** |
| **FL = Flat, PR = Prismatic, CH = Chipped or Broken, i = inclusion** *** excluded from average, stdev** | | | |

**Table 3: Comparison with other studies**

| This study: 108 grains, CT pixel 4-5 μm | | | | |
|---|---|---|---|---|
| | **Avg 3D/2D** | **1σ** | **% Diff Avg** | **1σ** |
| **Volume** | 0.82 | 0.22 | 23 | 16 |
| **Surface area** | 0.81 | 0.14 | 22 | 9 |
| **ESR** | 1.02 | 0.06 | 5 | 5 |
| **Mass** | 0.82 | 0.22 | 23 | 16 |
| **Ft** | 1.01 | 0.02 | 2 | 2 |
| Evans et al., 2008: 4 grains, CT pixel 3.77 μm | | | | |
| | **Avg 3D/2D** | **1σ** | **% Diff Avg** | **1σ** |
| **Volume** | 0.68 | 0.09 | 32 | 9 |
| **Surface area** | 0.77 | 0.08 | 23 | 8 |
| **ESR** | - | - | - | - |
| **Mass** | 0.66 | 0.08 | 34 | 8 |
| **Ft** | 0.93 | 0.10 | 7 | 10 |
| Glotzbach et al., 2019: 24 grains, CT pixel 1.2 μm | | | | |
| | **Avg 3D/2D** | **1σ** | **% Diff Avg** | **1σ** |
| **Volume** | 1.04 | 0.2 | 15 | 13 |
| **Surface area** | 1.12 | 0.17 | 16 | 14 |
| **ESR** | 0.93 | 0.06 | 8 | 5 |
| **Mass** | - | - | - | - |
| **Ft** | 0.99 | 0.02 | 2 | 2 |

**Appendix: Calculating ESR$_{FT}$, mean F$_T$, and eU**

*ESR$_{FT}$ and mean F$_T$*

      The starting point for calculating the equivalent-F$_T$ sphere radius (ESR$_{FT}$) when F$_T$ values are provided for each decay chain is the F$_T$ equation for a sphere (Farley et al., 1996; Ketcham et al., 2011):

$$F_T = 1 - \frac{3}{4}\frac{S}{R} + \frac{B}{16}\left(\frac{S}{R}\right)^3,$$ (A1)

where *R* is sphere radius, *S* is stopping distance, and *B* is an adjustment factor for the 3$^{rd}$-degree polynomial term to account for *S* being the weighted mean of stopping distances along branching decay chains, rather than a single stopping distance. For U and Th decay chains *B* should be 1.31, and for single stopping distances it should be 1 (Ketcham et al., 2011).

      Solving this equation for *S/R* over the F$_T$ range from 0.5 to 1 using a 3$^{rd}$-degree polynomial to match the effect of the cubic term gives:

$$\frac{S}{R} = 1.681 - 2.428F_T + 1.153F_T^2 - 0.406F_T^3 \ (B = 1.31)$$ (A2a)

$$\frac{S}{R} = 1.580 - 2.102F_T + 0.801F_T^2 - 0.279F_T^3 \ (B = 1)$$ (A2b)

The polynomial in Equation (A2a) is the appropriate one to use for data to be reported in age tables; Equation (A2b) is provided for completeness, and may be useful for comparing to other calculations that use mean *S* values to represent chains.

      The F$_T$ value to use is the weighted mean incorporating the separate factors F$_{T,238}$, F$_{T,235}$ and F$_{T,232}$, accounting for different alpha productivity along each chain. Expanding the approach of Farley (2002) to account precisely for $^{235}$U, we calculate:

$$A_{238} = (1.04 + 0.247[Th/U])^{-1}$$ (A3a)

$$A_{232} = (1 + 4.21/[Th/U])^{-1}$$ (A3b)

So that the weighted mean, $\overline{F_T}$, is

$$\overline{F_T} = A_{238}F_{T,238} + A_{232}F_{T,232} + (1 - A_{238} - A_{232})F_{T,235} \tag{A4}$$

S

olvin

g the result of Equation (A2) for $ESR_{FT}$ requires the analogous calculation to determine the weighted mean stopping distance, $\bar{S}$:

$$\bar{S} = A_{238}S_{238} + A_{232}S_{232} + (1 - A_{238} - A_{232})S_{235} \tag{A5}$$

5    where $S_{238}$, $S_{235}$, and $S_{232}$ are the weighted mean stopping distances for each decay chain (18.81 µm, 21.80 µm, and 22.25 µm, respectively, for apatite, but the calculation applies to any mineral).  Then, combining equations (A2) and (A5):

$$ESR_{FT} = \bar{S}/\left(\frac{S}{R}\right) \tag{A6}$$

*eU*

The earliest mention of *eU*, or effective uranium with respect to He production, we are
10   aware of is in Shuster et al. (2006), who put forward the formula

$$eU = [U] + 0.235[Th] \tag{A7}$$

where brackets indicate composition in ppm, without a detailed description of its derivation. Converting from elemental or isotopic compositions in ppm to an equivalent alpha particle production rate requires accounting for decay constants, isotopic proportions, alpha particle production, and atomic mass.  We calculate the present-day alpha production rate $R_\alpha$ (here
15   calculated in $\alpha$ g$^{-1}$ yr$^{-1}$) as:

$$R_\alpha = A\lambda pN/m_a \tag{A8}$$

where A is Avogadro's number, $\lambda$ is the decay constant, *p* is isotopic proportion, *N* is number of alpha particles produced in the decay chain, and $m_a$ is atomic mass.  The eU factor is then calculated by dividing the Th and Sm $R_\alpha$ by the combined U $R_{\alpha.}$ Utilizing the values in Table A1, we find the *eU* equation to be slightly different:

$$eU = [U] + 0.238[Th] + 0.0012[Sm] \quad (or\ 0.0083[^{147}Sm]) \tag{A9}$$

We do not know the reason for the small discrepancy with Equation (A7), but the ~1% difference in the effect of Th is not likely to be important for current uses of *eU*. The 0.238 factor has a likely uncertainty of ±0.002; the [232]Th half-life currently recommended by the nuclear chemistry community has only three significant figures based on a weighted average

5   of several determinations using different methodologies (Browne, 2006; Holden, 1990), whereas the geological community has adopted the value from the single study with the highest reported precision (Le Roux and Glendenin, 1963; Steiger and Jäger, 1977).

We include Sm for completeness, but as its alpha decay has a relatively low recoil energy it is not clear whether simply counting the particle is the most appropriate way to

10   include its potential contribution to damage which affects helium diffusivity. An alternative formulation can be posed in terms of energy deposition (kerma; Shuster and Farley, 2009):

$$R_k = A\lambda pNE/m_a \qquad (A10)$$

where *E* is the mean alpha particle recoil energy for the decay chain. The revised kerma-based quantity, $eU_k$, is then:

$$eU_k = [U] + 0.264[Th] + 0.0005[Sm] \quad (or\ 0.0034[^{147}Sm]) \qquad (A11)$$

This relation predicts that Sm will have an even lower relative contribution to diffusivity than

15   indicated in Equation (A9), but that Th will be 11% more potent, due to its higher mean recoil energy compared to [238]U. We do not currently recommend this approach, but it does pose a potentially testable hypothesis.

Browne, E. (2006), Nuclear Data Sheets for A = 232, Nuclear Data Sheets, 107, 2579-2648,

20   doi:10.1016/j.nds.2006.09.001.

Holden, N. E. (1990), Total half-lives for selected nuclides, Pure and Applied Chemistry, 62(5), 941-958, doi:10.1351/pac199062050941.

Le Roux, L. A., and L. E. Glendenin (1963), Half-life of 232Th, in Proceedings of the National Meeting on Nuclear Energy, Pretoria, South Africa, 83, 94.

Steiger, R. H., and E. Jäger (1977), Subcomission on geochronology: Convention on teh use of decay constants in geo- and cosmochronology, Earth Planet. Sci. Lett., 36, 359-362, doi:10.1016/0012-821X(77)90060-7.

5 **Table A1**: Values used for calculating eU

| | $^{238}$U | $^{235}$U | Th | Sm (total) | $^{147}$Sm |
|---|---|---|---|---|---|
| $\lambda^1$ (1/yr) | 1.55125E-10 | 9.8485E-10 | 4.9475E-11 | 6.539E-12 | 6.539E-12 |
| $p$ | 0.9928 | 0.0072 | 1 | 0.1499 | 1 |
| $m_a$ (g/mol) | 238.029 | 238.029 | 232.039 | 150.36 | 147 |
| $N$ ($\alpha$/chain) | 8 | 7 | 6 | 1 | 1 |
| $\alpha$/g/yr | 3.117E+12 | 1.256E+11 | 7.70E+11 | 3.93E+09 | 2.68E+10 |
| eU factor | | | 0.238 | 0.0012 | 0.0083 |
| | | | | | |
| $E$ (MeV) | 5.359 | 5.946 | 5.990 | 2.247 | 2.247 |
| energy deposited/g/yr | 1.671E+13 | 7.468E+11 | 4.61E+12 | 8.82E+09 | 6.02E+10 |
| eU$_k$ factor | | | 0.264 | 0.0005 | 0.0034 |

[1] Values for U and Th from Steiger and Jäger (1977).